


REPORT DOCUMENTATION PAGE			Form Approved OMB No. 0704-0188	
Public reporting burden for this collection of information is estimated to average 1 hour per response, including the time for reviewing instructions, searching existing data sources, gathering and maintaining the data needed, and completing and reviewing the collection of information. Send comments regarding this burden estimate or any other aspect of this collection of information, including suggestions for reducing this burden, to Washington Headquarters Services, Directorate for Information Operations and Reports, 1215 Jefferson Davis Highway, Suite 1204, Arlington, VA 22202-4302, and to the Office of Management and Budget, Paperwork Reduction Project (0704-0188), Washington, DC 20503.				
1. AGENCY USE ONLY (Leave blank)	2. REPORT DATE 18 August, 1995	3. REPORT TYPE AND DATES COVERED Technical 6/1/94 - 5/31/95		
4. TITLE AND SUBTITLE Substrate Effects on the Nanometer-Scale Mechanics of Gold Films		5. FUNDING NUMBERS N00014-93-1-1338		
6. AUTHOR(S) P. Tangyonyong, R. C. Thomas, J. E. Houston, T. A. Michalske, R. M. Crooks, A. J. Howard				
7. PERFORMING ORGANIZATION NAME(S) AND ADDRESS(ES) Department of Chemistry Texas A&M University College Station, Texas 77843-3255		8. PERFORMING ORGANIZATION REPORT NUMBER 14		
9. SPONSORING/MONITORING AGENCY NAME(S) AND ADDRESS(ES) Office of Naval Research 800 North Quincy Street Arlington, Virginia 22217-5000		10. SPONSORING/MONITORING AGENCY REPORT NUMBER		
11. SUPPLEMENTARY NOTES <i>J. Adhes. Sci. Technol.</i> 1994, 8, 897				
12a. DISTRIBUTION / AVAILABILITY STATEMENT Reproduction in whole, or in part, is permitted for any purpose of the United States Government. This document has been approved for public release and sale; it's distribution is unlimited.				
12b. DISTRIBUTION CODE				
13. ABSTRACT (Maximum 200 words) We have used interfacial force microscopy (IFM) and contact-mechanics analysis to quantitatively determine the deformation behavior and the mechanical properties of nanometer-size grains in polycrystalline Au films on various substrates. We evaluate these properties through an analysis of the loading-cycle curves and through a comparison of surface morphology before and after each nano-indentation measurement by constant repulsive-force imaging. All the Au surfaces were coated with self-assembling monolayers of <i>n</i> -octadecanethiol to passivate the adhesive interaction between the tungsten probe and Au surfaces. Our results show that both the deformation behavior and mechanical properties vary strongly as a function of substrate and these variations are mirrored by changes in such factors as the interfacial adhesion, grain size and shape, and the presence of grain-boundary impurities.				
DTIC QUALITY INSPECTED 8				
14. SUBJECT TERMS		15. NUMBER OF PAGES 36		
		16. PRICE CODE		
17. SECURITY CLASSIFICATION OF REPORT Unclassified	18. SECURITY CLASSIFICATION OF THIS PAGE Unclassified	19. SECURITY CLASSIFICATION OF ABSTRACT Unclassified	20. LIMITATION OF ABSTRACT	

Substrate Effects on the Nanometer-Scale Mechanics of Gold Films

P. Tangyonyong,¹ R. C. Thomas,² J. E. Houston,^{1*}
T. A. Michalske,¹ R. M. Crooks,^{2,3} and A. J. Howard¹

¹Sandia National Laboratories, Albuquerque, New Mexico

²Department of Chemistry, University of New Mexico,
Albuquerque, New Mexico

³Present Address: Department of Chemistry,
Texas A&M University, College Station, Texas

Accession For	
NTIS	CRA&I <input checked="" type="checkbox"/>
DTIC	TAB <input type="checkbox"/>
Unannounced <input type="checkbox"/>	
Justification _____	
By _____	
Distribution /	
Availability Codes	
Dist	Avail and/or Special
A-1	

Nm-Scale Mechanics of Au films

* Corresponding Author

Department 1114, Sandia National Laboratories,

P. O. Box 5800

Albuquerque, NM 87185

19950828 110

Abstract

We have used interfacial force microscopy (IFM) and contact-mechanics analysis to quantitatively determine the deformation behavior and the mechanical properties of nanometer-size grains in polycrystalline Au films on various substrates. We evaluate these properties through an analysis of the loading-cycle curves and through a comparison of surface morphology before and after each nano-indentation measurement by constant repulsive-force imaging. All the Au surfaces were coated with self-assembling monolayers of *n*-octadecanethiol to passivate the adhesive interaction between the tungsten probe and Au surfaces. Our results show that both the deformation behavior and mechanical properties vary strongly as a function of substrate and these variations are mirrored by changes in such factors as the interfacial adhesion, grain size and shape, and the presence of grain-boundary impurities.

Key Words: Interfacial force microscopy, Scanning probe microscopy,
Nano-mechanics, Mechanical properties of gold films.

I. Introduction

Recently, it has been reported that materials which are fabricated from nanometer-scale building blocks, i.e., the nano-phase materials, exhibit unique mechanical properties [1]. For example, composition-modulated thin films show a "supermodulus" effect for modulation wavelengths at the nm level [2]. Another example includes Al thin films with nanometer-scale Al_2O_3 precipitates formed by O ion implantation, which show a six-fold increase in the flow-stress threshold [3]. However, one of the limiting factor in the development of these materials involves the difficulty of performing mechanical-property measurements at this size level. In the present paper, we report the application of interfacial force microscopy (IFM) [4-6] to examine the deformation behavior and mechanical properties of nm-size grains in polycrystalline Au films on various substrates.

One of the most popular approaches for studying the mechanical properties of materials involves monitoring the loading behavior of the surface as it is elastically or plastically deformed by a probe, i.e., the indentation (loading-cycle) technique. Several techniques employ this approach for studying nanometer-scale materials. These include the ultra-microindenter [7], the nanoindenter [8], the atomic force microscope (AFM) [9] and the interfacial force microscope (IFM) [6]. The first two techniques evaluate the mechanical properties exclusively through an analysis of the loading-cycle behavior with force and deformation-displacement resolution in the 0.5 μN and 0.2 nm range, respectively. There is, however, no inherent imaging capability associated with these techniques, and it is not possible to monitoring changes in surface morphology after each nano-indentation

experiment. The analyses of the resulting deformations are often done *ex situ* by either optical means (for large indentations) or by scanning electron microscopy. In addition, the interfacial forces are generated by displacing a spring which means that the loading-cycle data are dominated by the energy stored in the elastic compliance of the spring.

In contrast, AFM is capable of monitoring the deformation processes following each load-cycle experiment through repulsive-force imaging. In addition, the force and displacement resolutions (1 nN and 0.1 nm) are smaller than either the ultra-microindenter or nanoindenter. However, AFM also suffers as a nano-indentation tool in that its force measurements are dominated by the energy stored in the elastic compliance of the displacement sensor.

IFM is a newly developing scanning-force technique. It is characterized by its use of a self-balancing force sensor, which is highly controllable and mechanically stable, with forces presently (both attractive and repulsive) measured at the tens of nN level and deformation displacement in the 0.1 nm range. It offers several important advantages over the AFM. For example, force and displacement can be measured in several modes, including constant force, constant force-rate, constant strain and constant strain-rate. Constant repulsive and attractive images can be obtained to aid in studying the deformation behavior, e.g., indentation sizes and shapes. In addition, large force loads (up to milli-newtons) can be delivered without sacrificing force resolution. The force-feedback detection scheme also decouples the sensor and sample responses so that force measurements are not dominated by the elastic compliance of the sensor. These features make IFM an exceptional nano-indentation tool which we demonstrate in the

present study.

Au films were chosen for this study because they are easily passivated with self-assembling monolayers, which prevents any probe-sample adhesion. This adhesion passivation is maintained even under large compressive stress [6] and allows the directly application of contact-mechanics analysis to quantitatively measure the mechanical properties from IFM data.

In this paper, we first present in detail the results for Au films on glass substrates, which show a wide range of deformation behavior and mechanical responses, some of which are not observed in the other systems. We then summarize the results for Au films on other substrates. These results are contrasted with those found on single-crystal Au(111) and discussed in terms of sample-substrate adhesion, grain morphology, and the presence of grain-boundary impurities.

II. Technical Details

A. Experimental

Polycrystalline Au films were prepared on four different types of substrates : glass, mica, and silicon(100) with both chromium and titanium adhesion layers. The thickness of all the Au films was ~ 200 nm. Au films on glass and mica were prepared by thermal-vapor deposition onto clean 300 C substrates at a rate of 0.2 nm/sec. The deposition was followed by a three-hour anneal at 275 C. Au/Cr/Si samples were prepared by thermal-vapor deposition of 10 nm of Cr onto clean 25 C Si(100) substrates at a rate of 0.5 nm/sec. This was followed by 200 nm of Au at the same temperature and

rate. Au/Ti/Si samples were prepared in the same manner using electron-beam vapor deposition. All the films, except for Au on mica, were subsequently cleaned by a brief exposure to a 3:1 concentrated H_2SO_4 : 30 % H_2O_2 solution. Self-assembling monolayers (SAM) were adsorbed onto the surface by soaking the gold films in 0.5 mM *n*-octadecanethiol solutions in purified ethanol for 36 hours. To ensure that the SAMs were uniform, they were characterized by ellipsometry and Fourier transform infrared external reflectance spectroscopy. For comparison, single-crystal Au(111) was also examined using the same cleaning and adsorption procedures as that of other substrates.

The tungsten probe was prepared by electrochemically etching a 0.1 mm wire in a potassium hydroxide (KOH) solution. The probe was characterized by scanning electron microscopy (SEM) and found to have a parabolic shape with apex radius of curvature of ~ 250 nm. All measurements were made with the same probe with both sample and probe immersed in hexadecane to eliminate capillary interactions.

IFM topological images were taken in the constant-repulsive-force mode at a load level of $0.5 \mu\text{N}$. To better evaluate the statistics of surface morphology, broader topological images were taken using a Nanoscope III AFM, which is capable of larger scan sizes (up to $100 \times 100 \mu\text{m}$) than those of IFM (up to $1 \times 1 \mu\text{m}$).

IFM loading-cycle experiments were performed using a force-feedback, constant strain-rate mode. The probe was first placed over the center of a selected grain and the surface was then moved toward the probe at a rate of 20 nm/sec . At a predetermined repulsive load, the surface was withdrawn at the same rate. This produces a loading-cycle curve where contact is defined

as the point where the load begins to go repulsive.

B. Data Analysis

A loading-cycle curve consists of two portions, the loading (approach) and the unloading (withdrawal), as illustrated for single-crystal Au(111) sample (Fig. 1). Referring to Fig. 1, there are two regions in the loading curve. Region 1 is an elastic region, which is described by the classical Hertzian model (shown as the solid line in Fig. 1) for a rigid, non-interacting parabolic probe deforming an elastic half space [10]. For small displacements, the tip of the parabolic probe can be approximated as that of a sphere, and the relationship between load and displacement as the surface is elastically deformed is given by [11]

$$F = \frac{4}{3} * \sqrt{R} * E_r * D^{\frac{3}{2}}, \quad (1)$$

where F is the applied load; R is the probe-tip radius of curvature, and D is the surface displacement. E_r is the composite elastic modulus (Young's modulus) of the probe and sample, defined by [11]

$$\frac{1}{E_r} = \frac{1 - \nu_s^2}{E_s} + \frac{1 - \nu_i^2}{E_i}, \quad (2)$$

where ν is Poisson's ratio, and subscripts s and i refer to the sample and the probe, respectively.

The point at which the loading curve deviates from the Hertzian model marks the threshold for plastic deformation (region 2 in Fig. 1), and the maximum shear stress at the threshold for plastic deformation can be calculated from the continuum elastic theory [11] using the threshold force value. For gold, this value (S) is calculated to be

$$S = 0.31 * \left(\frac{1.5 * F_t}{\pi a_t^2} \right), \quad (3)$$

where a is the projected contact radius, and the subscript t denotes the threshold value from the loading curve. The value of a for a spherical probe is obtained through the relationship

$$a = \sqrt{RD}. \quad (4)$$

If an indentation is created during the loading cycle, the initial linear region in the unloading curve, as illustrate in region 3 of Fig. 1, can be modeled by Sneddon's analysis of surface stiffness based on the assumption that the contact area remains constant, i.e., the probe is embedded in a permanently deformed socket [12]. The surface stiffness can be written as [12]

$$\frac{dF}{dD} = \frac{2}{\pi} \sqrt{A} * E_r, \quad (5)$$

where A is the projected contact area given by,

$$A = \pi R D_p, \quad (6)$$

where D_p is the plastic depth of the indentation, i.e., the depth of the probe in contact with the sample under load [8]. D_p is larger than the final depth (D_F), i.e., the relaxed depth of the indentation after removal of the probe, by ΔD [8]. To determine the plastic depth, we first measure the final depth, which is determined by taking the difference between the line scans of the topological images before and after the loading-cycle experiment. Next, we find ΔD , as demonstrated in Fig. 1, by fitting the linear portion of the unloading curve at the high loading values and extrapolating to zero load [8]. ΔD is then the difference between the x intercept of the linear fit and the zero-load point of the unloading curve.

III. Results

A. Au/Glass

In this paper, we present a detailed discussion of the results on the Au/glass system because it shows a wide range of deformation behavior and

mechanical responses that are not readily observed in the other systems.

One of the interesting features in this system is its surface morphology, which is shown in the AFM image in Fig. 2. The Au surface is dominated by large flat grains with a narrow distribution of grain sizes averaging ~ 500 nm in diameter. Occasionally, we also see grains that protrude above the nominally flat surface by an average of 10 to 30 nm (these appear as bright spots in Fig. 2). The mean roughness of this surface is ~ 4.1 nm, with a maximum-minimum deviation of ~ 102 nm. The large ratio of maximum-minimum deviation to mean surface roughness is a result of the presence of the protruding grains. In this section, we first focus on the behavior of the protruding grains because they show the full range of deformation response encountered in these films, and then we present the results of a general survey for typical non-protruding grains.

The loading-cycle data for a typical grain protruding from the average surface by ~ 10 nm, which is shown in the IFM repulsive-force image of Fig. 3(a), is displayed in Fig. 4(a). The results are dominated by a large hysteresis loop between loading and unloading. Detailed analysis reveals that there are three distinct regions in the loading portion of Fig. 4(a). In the first region, we find no hysteresis for peak loads less than ~ 6 μ N. In addition, the relationship between load and deformation closely follows the classical Hertzian model (Eq. (1)), shown as the solid line in Fig. 4(a). Thus, we are elastically deforming the surface in region 1.

The point at which the loading curve deviates from the Hertzian behavior occurs at a load of ~ 6 μ N (beginning of region 2). Above ~ 27 μ N (region 3), the hysteresis loop closes and the deformation is again elastic, as born out by the Hertzian fit shown as the solid line in region 4.

Starting at the maximum load in region 4, the unloading curve consists of two distinct Hertzian-like regions (4 and 5 in Fig. 4(a)), which are separated at a load of $\sim 6 \mu\text{N}$. Region 5 has the same elastic properties as region 1. Quantitatively, the effective moduli of regions 1 and 3 derived from Hertzian analysis (Eq. (1)) are found to be 28 and 66 GPa, respectively.

After the loading cycle of Fig 4(a), a repulsive-force image (Fig. 3(b)) was taken to clarify the nature of plastic deformation seen in Fig. 4(a). The image clearly shows that the grain has not been indented but rather has been displaced into the surface by the probe, which suggests the availability of sub-surface free volume. Line scans across the center of the images indicate a total grain displacement of $\sim 8 \text{ nm}$.

Repeating the loading procedure of Fig. 4(a) to a higher peak load results in the load-displacement of Fig. 4(b), which shows a hysteresis loop and five distinct regions of deformation behavior. Regions 1 and 2 are identical to regions 4 and 5 of the initial loading cycle of Fig. 4(a). The onset of plastic deformation (region 3) occurs at a load of $\sim 44 \mu\text{N}$, and the maximum shear stress at the threshold for plastic deformation is calculated to be 2.6 GPa.

Since region 4 shows no indication of loop closure at higher loads, we associate this deformation with an actual indentation of the grain itself. This assessment is confirmed by the image taken after the second loading cycle Fig. 3(c), and the depth of the indentation is found to be $\sim 5 \text{ nm}$. Since an indentation has been created, Eq. (5) can be used to analyze the initial portion of the unloading curve (region 4). The result is shown as a dashed line in region 4 of Fig. 4(b). Using Eqs. (5)-(6), the effective elastic constant of this region is calculated to be 79 GPa. Region 5 has a Hertzian-like appearance

and is representative of the last stages of elastic relaxation as the probe is removed from the indentation [13].

A general survey of several non-protruding grains (Table I) gives the values of 75 ± 15 , 64 ± 16 and 2.7 ± 0.5 GPa for the elastic moduli (during the loading and unloading) and the maximum shear stress at the plastic threshold, respectively. These values agree reasonably well with those obtained for Au(111) (70 ± 6 , 53 ± 5 and 2.9 ± 0.1 GPa) and with the protruding grain when it is in contact with the glass substrate (66, 79 and 2.6 GPa). The elastic modulus during the loading is also in good agreement with the tabulated value for solid Au (78 GPa) [14].

B. Au/Mica

The AFM images show that the Au films on mica substrates are dominated by large rounded grains averaging ~ 250 nm in diameter (Fig. 5). The overall mean surface roughness is ~ 5.4 nm, with a maximum-minimum deviation of ~ 52 nm. In contrast to the Au/glass system, we find no protruding grains on this substrate. The loading-cycle curves for this system, an example of which is shown in Fig. 6, exhibit a simple behavior similar to that seen for Au(111) in Fig. 1. A general survey of this surface (Table I) shows that the values of the elastic moduli (during the loading and unloading) and the maximum shear stress at the plastic threshold are 36 ± 5 , 43 ± 8 and 1.7 ± 0.2 GPa, respectively.

C. Au/Cr/Si(100) and Au/Ti/Si(100)

The Au/Cr/Si and Au/Ti/Si systems were prepared at room temperature without any post-deposition annealing, and the AFM images (Figs. 7-8) show that the Au films are dominated by small grains with narrow distributions of grain diameters averaging ~ 150 nm and ~ 60 nm for Au/Cr/Si and Au/Ti/Si, respectively. The values of the mean surface roughness are ~ 2.4 and 1.8 nm with maximum-minimum deviations of ~ 24 and ~ 16 nm, respectively. Differences in the surface morphology between these two systems perhaps reflect differences in the deposition methods : thermal evaporation for Au/Cr/Si versus e^- -beam for Au/Ti/Si. Furthermore, the images show no evidence of protruding grains on either of the surfaces or evidence of grain-boundary sliding or grain sagging. Thus, the loading-cycle results, typified by the behavior of Au/Cr/Si(100) shown in Fig. 9, have a simple form similar to that seen for Au(111) in Fig. 1. Quantitatively, a general survey of the Au/Cr/Si surface (Table I) show that the values of the elastic moduli (during loading and unloading) and the maximum shear stress at the plastic threshold (Table I) are 110 ± 19 , 135 ± 16 , and 4.5 ± 0.4 GPa, respectively; and the values for the Au/Ti/Si (Table I) are 48 ± 5 , 78 ± 7 , and 2.1 ± 0.3 GPa, respectively.

IV. Discussion

For the Au/glass system, the protruding grains exhibit a broad range of deformation responses that are not encountered on non-protruding grains or for the grains of other systems. The use of IFM and contact mechanics, however, enable us to identify the full range of inter- and intra-granular deformations on the basis of the loading-cycle data and the images before and

after the loading-cycles. As an example, a schematic model summarizing the deformation behavior of the protruding grain shown in Fig. 3(a) during the loading-cycle of Fig. 4(a) is presented in Fig. 10(a).

Referring to region 1 in Fig. 10(a), the grain is elastically deformed by the probe, slightly sagging under the applied load. The elastic sagging can be modeled by a diaphragm loaded by a probe [15] whose contact area varies with load and which become appreciable with respect to the grain size. The apparent smaller value of the measured effective elastic constant (28 GPa) reflects the contribution from the elastic sagging.

As the load is increased above $\sim 6 \mu\text{N}$ (region 2), the grain slips at its boundary, allowing it to slide into the surface and reduce the sub-surface free volume. Concurrent with the inter-granular displacement, the sagging increases with increasing load and the grain is further elastically deformed. This process continues until the grain comes into contact with the glass substrate, which marks the beginning of region 3.

In region 3, we see only elastic deformation, and there is no further grain-boundary sliding or grain sagging. The elastic behavior here is quite different from region 1, as evidenced by the large increase in the measured elastic modulus (from 28 to 66 GPa). In region 4, the grain recovers from the elastic strain of region 2 and 3 while remaining in contact with the substrate. As the load is decreased further (region 5), the grain partially rebounds from the sagging imposed in regions 1 and 2. Subtracting the line-scan displacement ($\sim 8 \text{ nm}$) from the loading displacement ($\sim 12 \text{ nm}$) gives a total rebound of $\sim 4 \text{ nm}$ in region 5. Our conclusion concerning this behavior is supported by the fact that the effective elastic constant from the Hertzian analysis in region 5 is the same as that determined in region 1.

Likewise, the deformation modes in the second loading cycle of Fig. 4(b) are summarized in Fig. 10(b). The grain is deformed elastically with slight sagging into the remaining free volume (region 1), until contact is again made with the substrate (beginning of region 2). In region 2, we only see elastic deformation. As expected, the elastic behavior of these two regions is the same as regions 4 and 5 during the first loading cycle. Higher loading results in the creation of a ~ 5 nm indentation (region 3).

In region 4, the probe is embedded in a permanently deformed indentation and the contact area initially remains constant as the probe is removed [12]. In region 5, we observe an elastic behavior which results from the final stages of probe removal from the indentation [13].

The loading-cycle curve of a typical non-protruding grain is shown in Fig. 11. We do not observe any grain-boundary sliding or grain sagging. The grain is first elastically deformed by the probe until the load exceeds the threshold value for plastic deformation, resulting directly in the creation of an indentation. The unloading curve shows a typical two-region behavior. The initial region has a linear characteristic resulting from the constant contact area between the probe and the sample. This is followed by a region of elastic recovery as the probe withdraws from the indentation.

The existence of protruding grains with free volume beneath is a sign of early-stage delamination. Au films do not adhere well to glass substrates and peel if immersed in the H_2SO_4 : 30 % H_2O_2 cleaning solution for extended periods. It is most likely that our brief surface cleaning procedure triggers the early stages of this delamination.

There is no evidence of protruding grains or grain sagging on other systems. The loading-cycle curves show a simple behavior similar to that for

Au(111) (Fig. 1). On mica substrates, the values of the measured elastic properties are, however, much smaller than those for Au(111). Perhaps, these deviations are due to the poor interfacial adhesion between Au and the mica substrate; Au peels easily from the mica substrate using adhesive tape and delaminates instantly if immersed in the $\text{H}_2\text{SO}_4 : 30\% \text{H}_2\text{O}_2$ cleaning solution. The poor wetting leads to the formation of rounded islands during the deposition, which eventually coalesce to form a continuous film. The spherical nature of the grains implies that, during the loading-cycle experiment, the applied load causes deformations at both the probe-Au and Au-mica interfaces. In other words, there is a change in the contact area with increasing load at both interfaces. Thus, the measured surface displacement (D) contains a component from the deformation at the Au-mica interface, and the apparent smaller values of the measured elastic properties reflect the contribution of this component.

In contrast, the grain shapes for the Au/Cr/Si and Au/Ti/Si systems are not as round as those for Au/mica and the average grain size is also much smaller. In addition, the interfacial Au-substrate adhesion in both systems is so strong in that Au does not peel from the substrates using adhesive tape and does not delaminate even if immersed in the $\text{H}_2\text{SO}_4 : 30\% \text{H}_2\text{O}_2$ cleaning solution for extended periods. Besides the strong interfacial adhesion, Cr and Ti are known to diffuse through the Au layer along the grain-boundaries and segregate at the surface [16]. The strong interfacial adhesion and the presence of Cr and Ti impurities at the grain-boundary surfaces significantly affect the mechanical properties of the Au films as evidenced by the large variation in the values of elastic properties for these films in comparison with Au(111).

Interestingly, all of the thin Au films display stick-slip motion (the serrated behavior in the loading-cycle curves) to varying degrees when they are plastically deformed by the probe. The magnitude of the stick-slip is, however, most pronounced for Au films on glass substrates (Fig. 11) and smallest for films on Si substrates with an adhesion layer (Fig. 9). The observation of these individual stick-slip events is made possible by the small elastic compliance of the IFM force sensor. These events are not observed by either the nanoindenter or AFM because the large elastic compliance of the sensor makes constant-strain rate measurements impossible. Equally interesting are the changes in the values of elastic moduli after these films are plastically indented by the probe. These changes are manifested as differences in the values between elastic moduli during loading and unloading (Table I). The changes also vary from one substrate to the other and do not show any specific trend. For example, the loading value is larger than the unloading one for the Au/glass system and smaller for Au/Cr/Si.

V. Conclusion

In this paper, we have demonstrated the use of the IFM and contact-mechanics analysis to follow the detailed deformation behavior of nm-size grains in thin Au films on several substrates and to quantitatively determine their mechanical properties. In addition, we have shown that the deformation behavior and mechanical properties of the films vary significantly from one substrate to the other. These variations are accompanied by changes in such factors as the interfacial adhesion, grain morphology and the presence of grain-boundary impurity atoms. In order to

delineate these various effects, it will be necessary to perform experiments such as probing the mechanical properties as a function of grain size and as a function of controlled level of various types of grain-boundary impurities (e.g., Au/Si(100) in the absence of adhesion layers). Besides these specific substrate effects, it should also be easy to extend our measurements to examine the effect of other factors, such as temperature and film thickness. These experiments should substantially contribute to the understanding of inter- and intra-granular deformation mechanisms such as, grain-boundary sliding, slip and twinning. Significant insight should also be obtained in the role of inter-defect interactions (e.g., dislocation-dislocation interactions and interactions between point defects and dislocations) in modifying the mechanical properties of thin films. This kind of information is crucial in developing an understanding of the mechanical behavior and, hence, tailoring the mechanical properties of nanophase materials.

Acknowledgment

This Sandia portion of this work is supported by the Office of Basic Energy Sciences, Division of Material Sciences, U.S. Department of Energy under Contract No. DE-AC04-76DP00789. R.C.T acknowledges the support of the Association of Western Universities, and R.M.C is supported by the Office of Naval Research.

References

1. R. W. Siegel, Ann. Rev. Material Sci. 21, 559-578 (1991).
2. R. C. Cammarata, Scripta Metall. 20, 479-486 (1986).
3. R. J. Bourcier, D. M. Follstaedt, M. T. Dugger and S. M. Myers, Nuclear Instr. Methods in Phys. Res. B59/60, 905-908 (1991); and D. M. Follstaedt, S. M. Myers and R. J. Bourcier, Nuclear Instr. Methods in Phys. Res. B59/60, 909-913 (1991).
4. S. A. Joyce and J. E. Houston, Rev. Sci. Instru. 62, 710-715 (1991).
5. J. E. Houston and T. A. Michalske, Nature 356, 266-267 (1992).
6. R. C. Thomas, J. E. Houston, T. A. Michalske, and R. M. Crooks, Science 259, 1883-1885 (1993).
7. T. J. Bell, A. Bendeli, J. S. Field, M. V. Swain, and E. G. Thwaite, Metrologia 28, 463-469 (1991).
8. M. F. Doerner and W. D. Nix, J. Mater. Res. 1, 601-609 (1986).
9. M. Salmeron, A. Folch, G. Neubauer, M. Tomitori, D. F. Ogletree, and W. Kolbe, Langmuir 8, 2832-2842 (1992).
10. I. N. Sneddon, Int. J. Eng. Sci. 3, 47-58 (1965).
11. S. P. Timoshenko and J. N. Goodier, Theory of Elasticity, chapter 12. McGraw-Hill, New York (1970).
12. G. M. Pharr, W. C. Oliver, and F. R. Brotzen, J. Mater. Res. 7, 613-617 (1992).
13. J. S. Field and M. V. Swain, J. Mater. Res. 8, 297-306 (1993).
14. R. W. Hertzberg, Deformation and Fracture Mechanics of Engineering Materials, chapter 1. John Wiley & Sons, New York (1976).
15. A. Blake, Handbook of Mechanics, Materials and Structures, pp. 615-

619. John Wiley & Sons, New York (1985).
16. P. H. Holloway, D. E. Amos, and G. C. Nelson, J. App. Physics **47**, 3769-3775 (1976).

Table I : Summary of the statistics of surface morphology and the mechanical properties of polycrystalline gold films on various substrates. As a reference, single-crystal Au(111) data are also tabulated.

Sample	Average Grain Diameter (nm)	Mean Surface Roughness (nm)	Minimum-Maximum deviation (nm)	Elastic Modulus (loading) (GPa)	Elastic Modulus (unloading) (GPa)	Maximum Shear Stress at the Plastic Threshold (GPa)
Au/Glass	500	4.1	102	75 ± 15	64 ± 16	2.7 ± 0.5
Au/Mica	250	5.4	52	36 ± 5	43 ± 8	1.7 ± 0.2
Au/Cr/Si(100)	150	2.4	24	110 ± 19	135 ± 16	4.5 ± 0.4
Au/Ti/Si(100)	60	1.8	16	48 ± 5	78 ± 7	2.1 ± 0.3
Au(111)				70 ± 6	53 ± 5	2.9 ± 0.1

Figure Captions

- Fig. 1 A typical loading-cycle curve for single-crystal Au(111). The solid line represents the fit based on the Hertzian model for a parabolic punch deforming an elastic half space [10]. The point at which the loading curve deviates from Hertzian marks the threshold for plastic deformation. The dashed line represents an analysis of the unloading curve based on Sneddon's model of a parabolic punch embedded in an indentation [12].
- Fig. 2 2500 x 2500 nm AFM repulsive-force image of a Au film grown on a glass substrate. The surface is dominated by large flat grains with average diameter of ~500 nm with a few grains protruding above the nominal flat surface by an average of 10 to 30 nm (these appear as bright spots in the image).
- Fig. 3 400 x 400 nm IFM repulsive-force images of a typical protruding grain (a) before loading, (b) after a loading cycle to a peak load of ~ 35 μN , and (c) after a second loading cycle to a peak load of ~75 μN .
- Fig. 4 (a) Loading-cycle data taken at the center of the protruding grain shown in Fig. 3a to a peak load of ~ 35 μN . Solid lines represent the fits based on the Hertzian model; (b) Loading-cycle taken at the same position to a peak load of ~ 75 μN . The dashed curve represents the analysis based on constant contact area between the probe and the indentation.

Fig. 5 2500 x 2500 nm AFM repulsive-force image of a Au film grown on a mica substrate with an average grain diameter and a mean surface roughness of ~ 250 nm and ~ 5.4 nm, respectively.

Fig. 6 A typical loading-cycle curve taken at the center of a grain on a mica substrate, which has been plastically indented by the probe. The solid line represents the fit based on the Hertzian model for a parabolic punch deforming an elastic half space. The dashed line represents an analysis of the unloading curve based on Sneddon's model of a parabolic punch embedded in an indentation.

Fig. 7 2500 x 2500 nm AFM repulsive-force image of the Au/Cr/Si surface with with an average grain diameter and a mean surface roughness of ~ 150 nm and ~ 2.4 nm, respectively.

Fig. 8 2500 x 2500 nm AFM repulsive-force image of the Au/Ti/Si surface with with an average grain diameter and a mean surface roughness of ~ 60 nm and ~ 1.8 nm, respectively.

Fig. 9 A typical loading-cycle curve of the Au/Cr/Si surface. The solid line represents the fit based on the Hertzian model for a parabolic punch deforming an elastic half space. The dashed line represents an analysis of the unloading curve based on Sneddon's model of a parabolic punch embedded in an indentation.

Fig. 10 A schematic model of the behavior of the protruding grain shown in Fig. 4(a). Arrows indicate the direction of motion of the probe. (a) and (b) refer to the different regions shown in Fig. 4(a) and 4(b), respectively.

Fig. 11 A typical loading-cycle curve for a non-protruding grain, which has been plastically indented by the probe. The solid line represents the

fit based on the Hertzian model for a parabolic punch deforming an elastic half space. The dashed line represents an analysis of the unloading curve based on Sneddon's model of a parabolic punch embedded in an indentation.

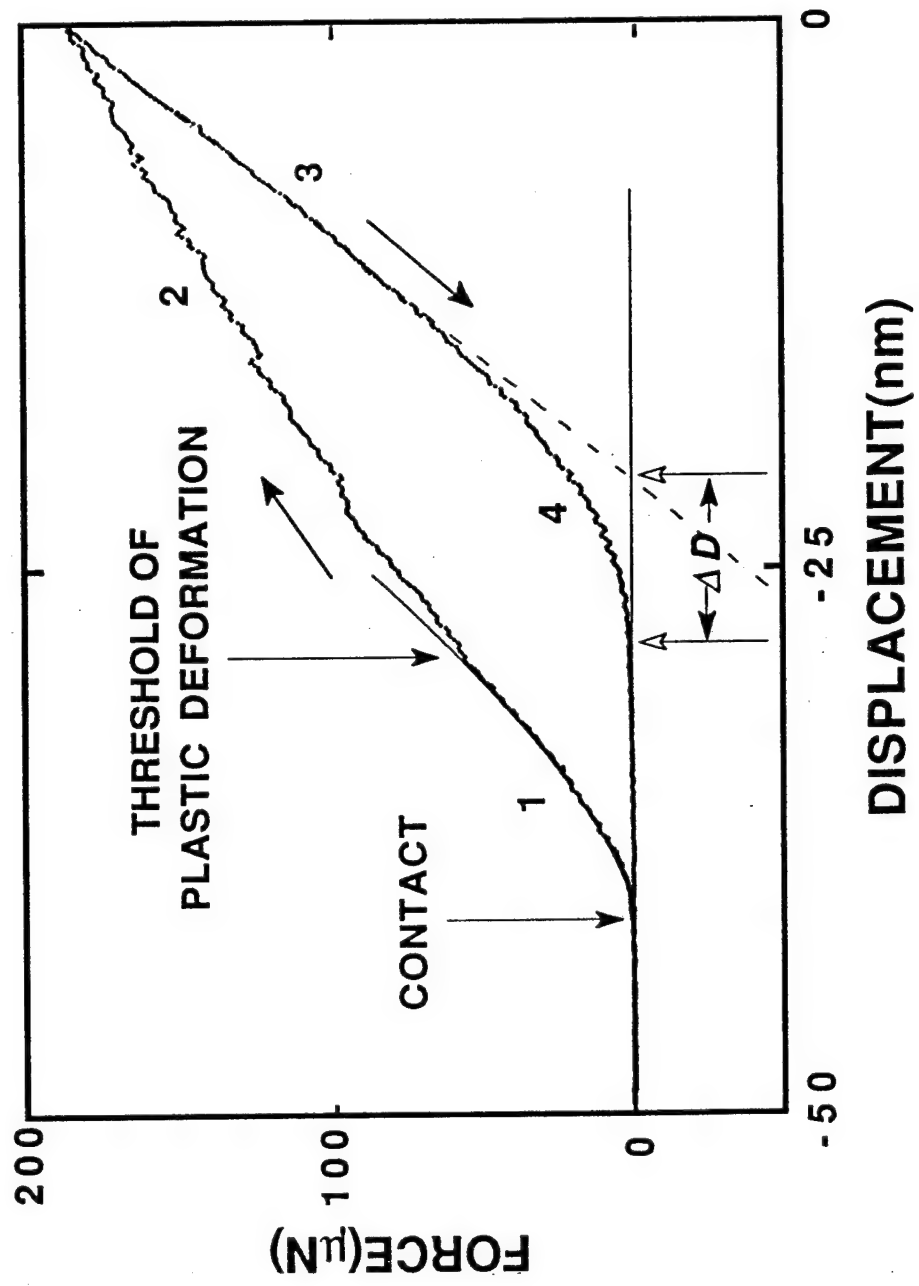


Fig. 1

Fig. 2

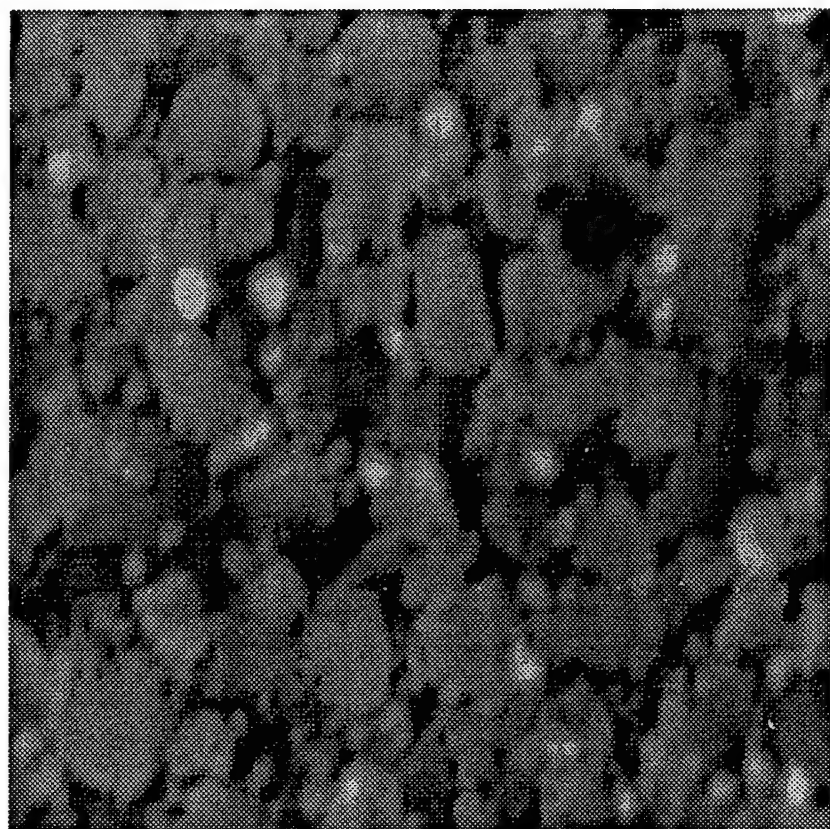


Fig. 3



(a)



(b)



(c)

Fig. 4

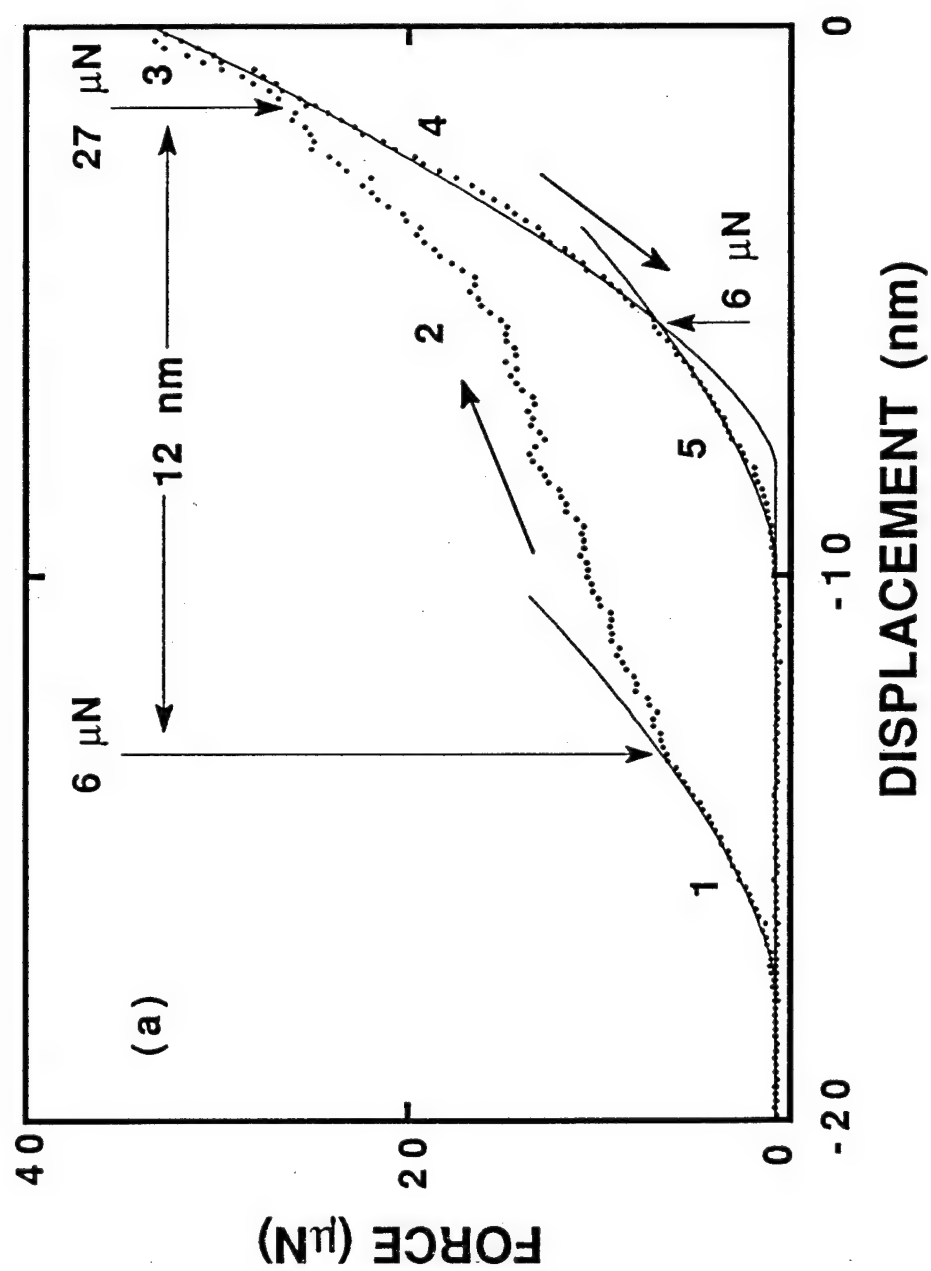


Fig. 5

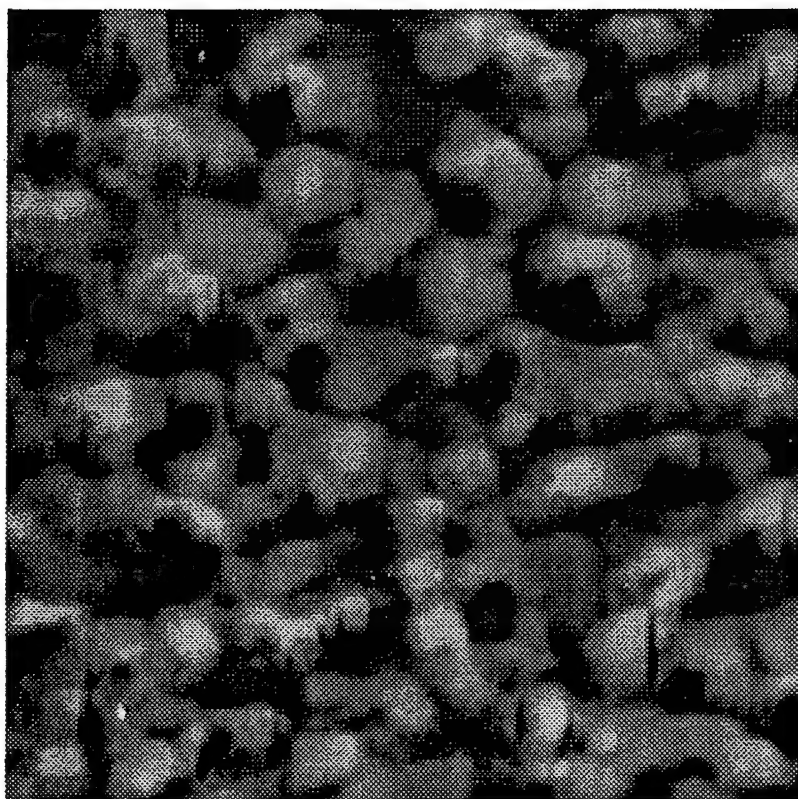


Fig. 6

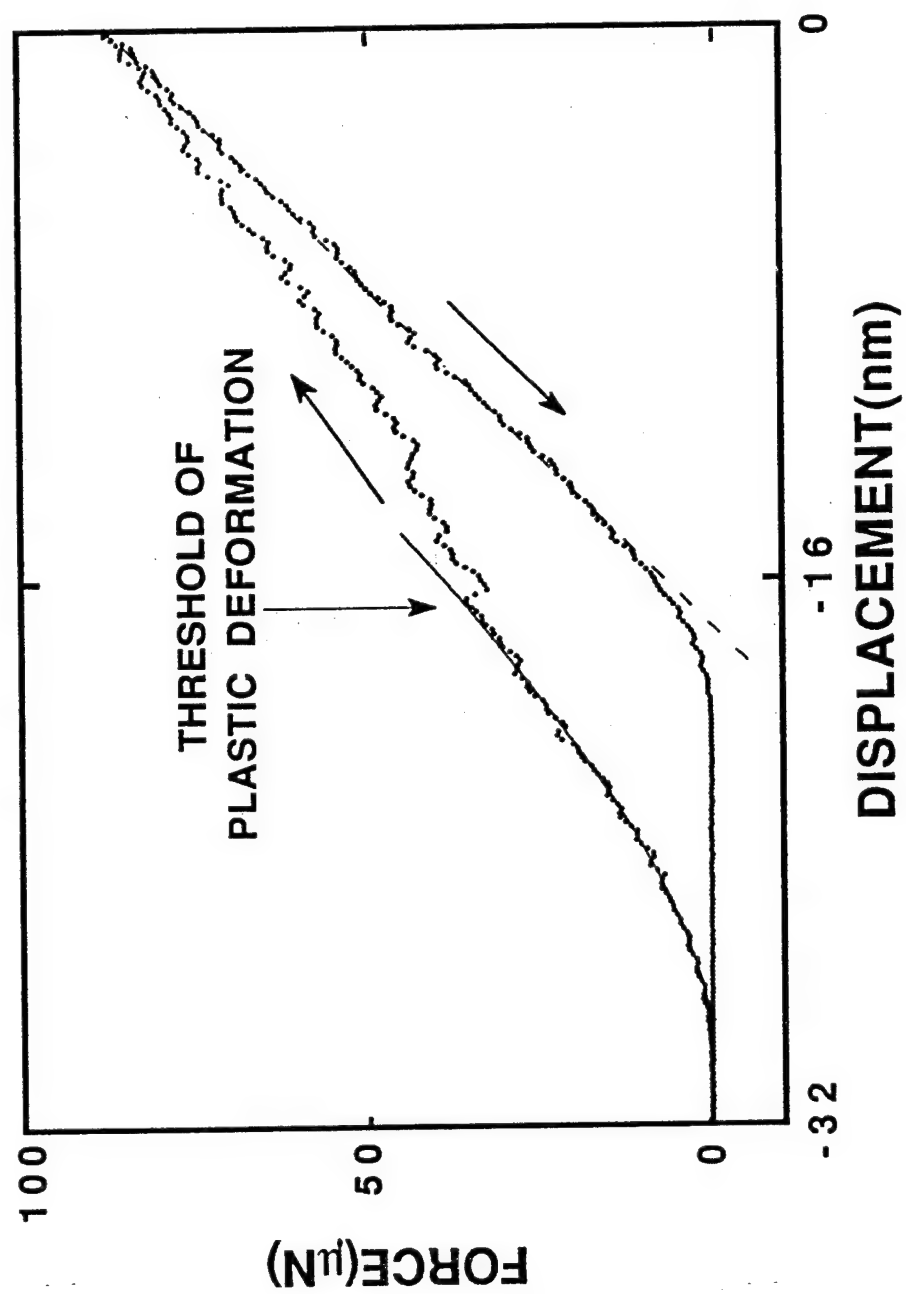


Fig. 7

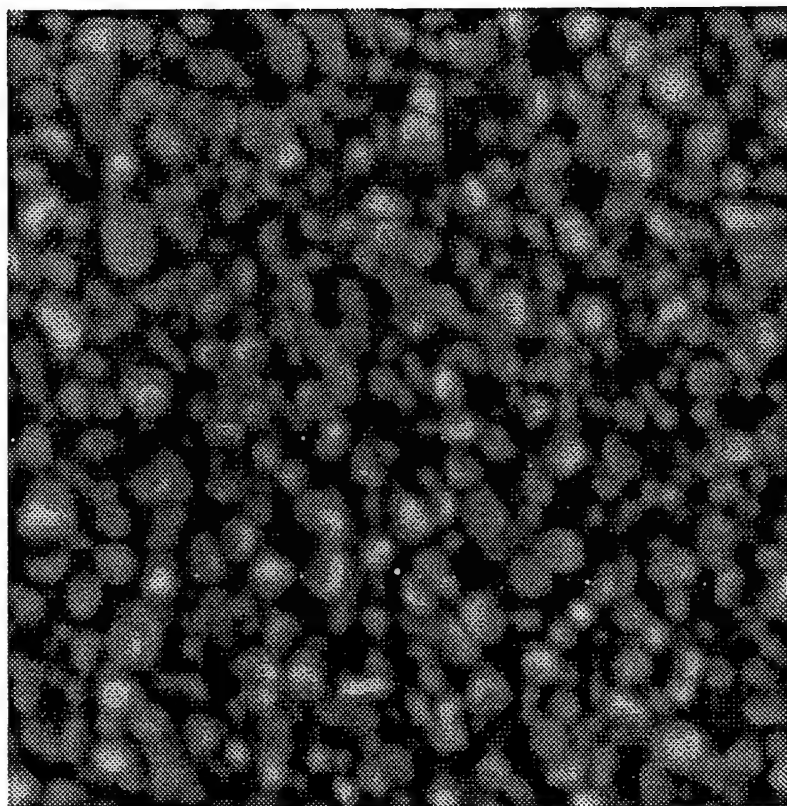


Fig. 8

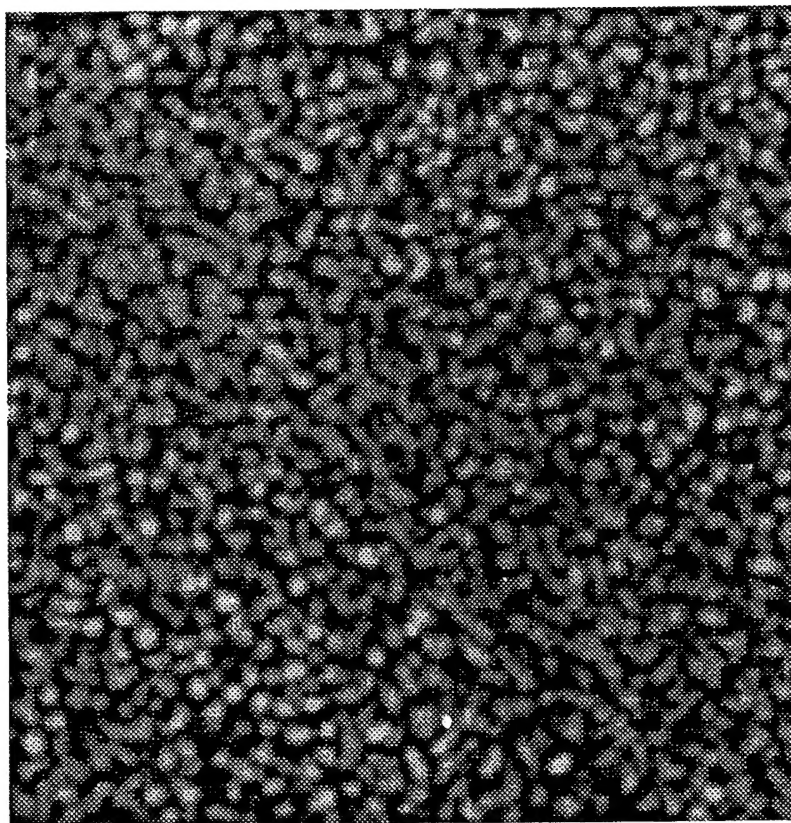


Fig. 9

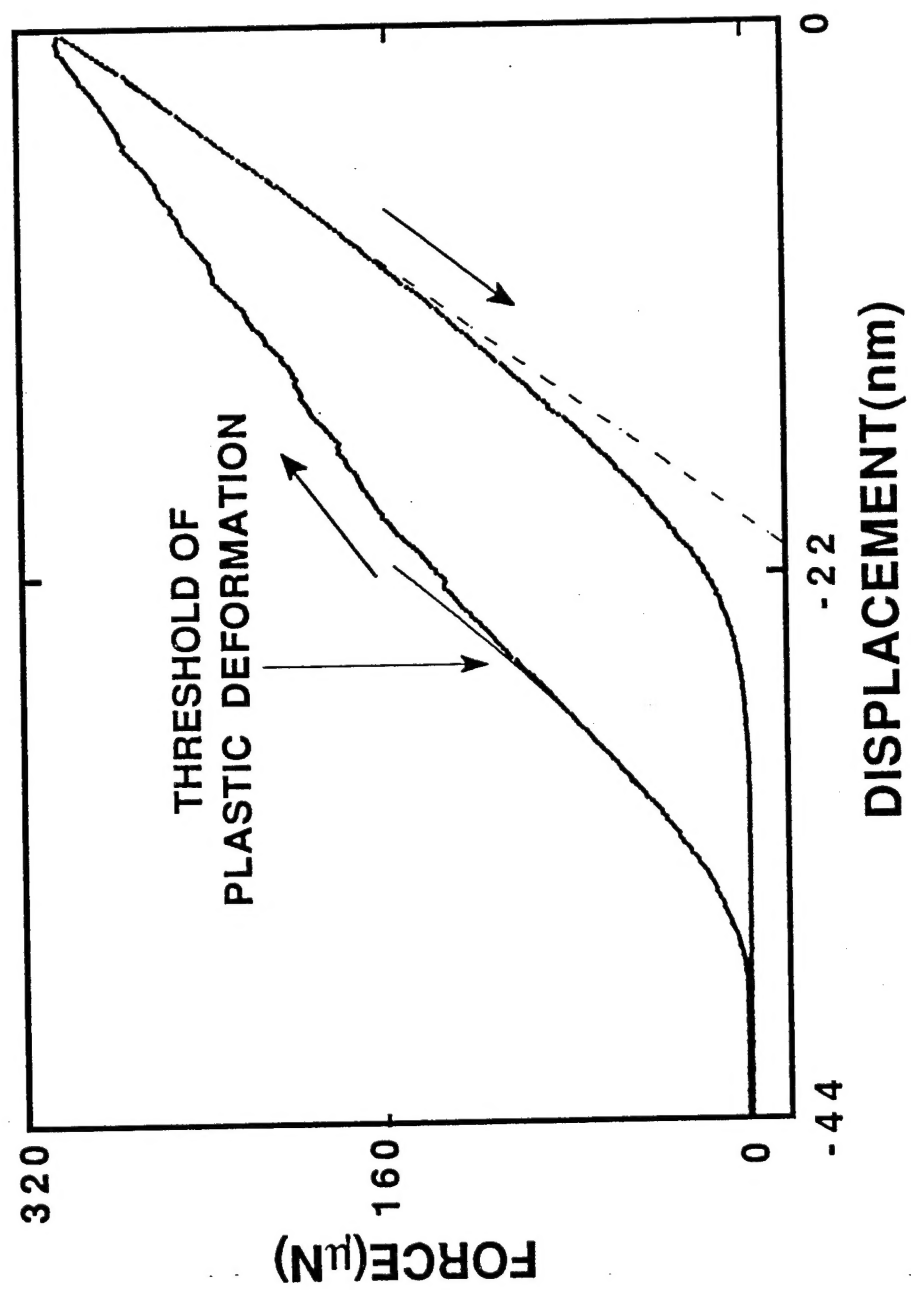


Fig. 10

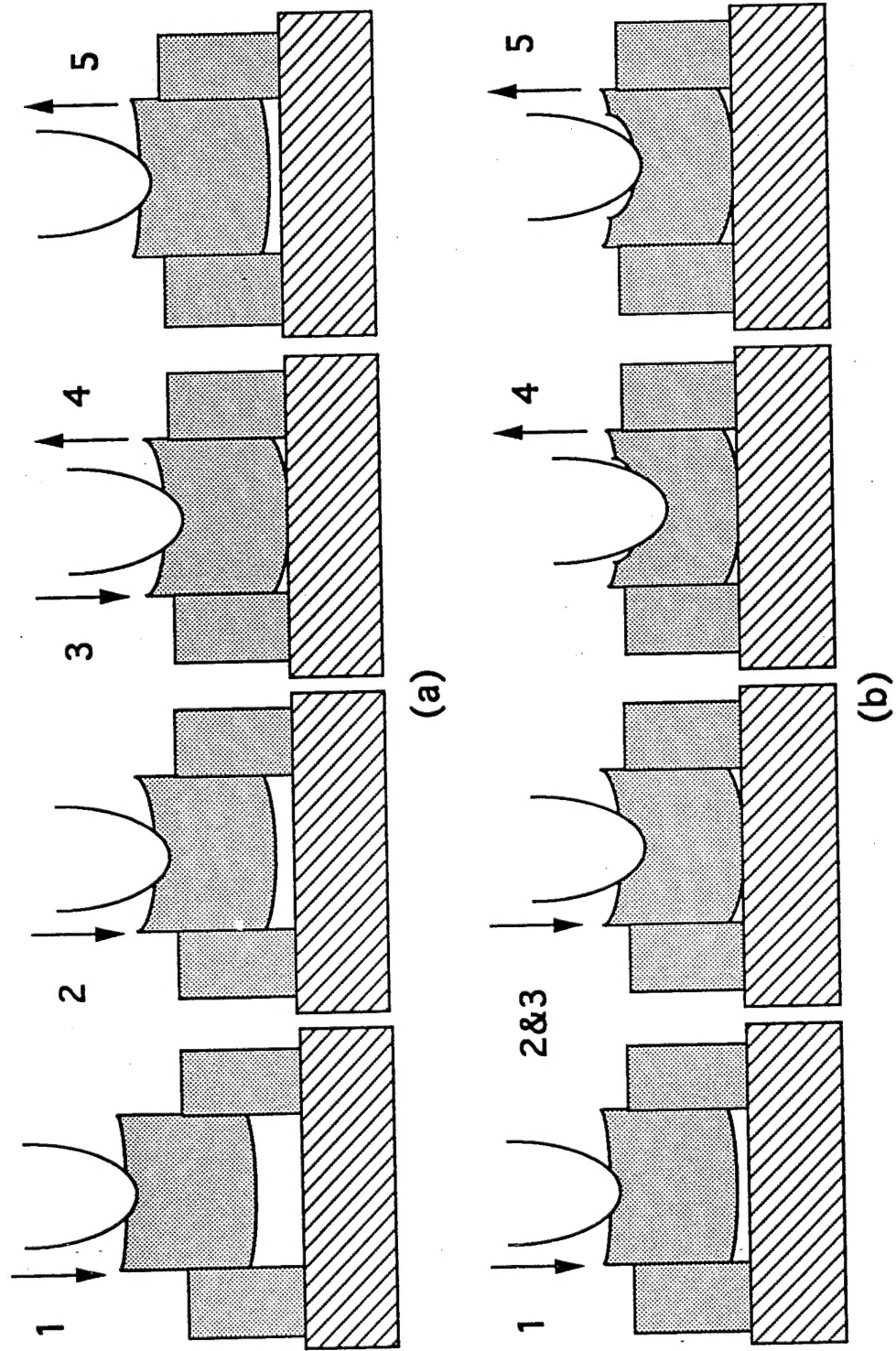


Fig. 11

